Open Research Online

The Open University's repository of research publications and other research outputs

A notch filter for ship detection with polarimetric SAR data

Journal Item

How to cite:

Marino, Armando (2013). A notch filter for ship detection with polarimetric SAR data. IEEE Journal of Selected Topics in Applied Earth Observation and Remote Sensing, 6(3) pp. 1219–1232.

For guidance on citations see FAQs.

© 2013 IEEE

Version: Accepted Manuscript

Link(s) to article on publisher's website:
http://dx.doi.org/doi:10.1109/JSTARS.2013.2247741

Copyright and Moral Rights for the articles on this site are retained by the individual authors and/or other copyright owners. For more information on Open Research Online's data policy on reuse of materials please consult the policies page.

oro.open.ac.uk

A Notch Filter for Ship Detection with Polarimetric SAR Data

Armando Marino, *Member, IEEE*

Abstract

Ship detection with Synthetic Aperture Radar (*SAR*) is a major topic for the security and monitoring of maritime areas. One of the advantages of using SAR lay in its capability to acquire useful images with any-weather conditions and at night time. Specifically, this paper proposes a new methodology exploiting polarimetric acquisitions (dual- and quad-polarimetric).

The methodology adopted for the detector algorithm was introduced by the author and performs a perturbation analysis in space of polarimetric targets checking for coherence between the target to detect and its perturbed version on the data. In the present work, this methodology is optimized for detection of marine features. In the end, the algorithm can be considered to be a negative (notch) filter focused on sea. Consequently, all the features which have a polarimetric behavior different from the sea are detected (i.e. ships, icebergs, buoys, etc). Moreover, a dual polarimetric version of the detector is designed, to be exploited in the circumstances where quad polarimetric data cannot be acquired.

The detector was tested with TerraSAR-X quad polarimetric data showing significant agreement with the available ground truth. Moreover, the theoretical performances of the detector are tested with Monte Carlo simulations in order to extract the probabilities of detection and false alarm. An important result is that the detector is, up to some extend, independent of the sea conditions.

Keywords

Synthetic Aperture Radar, Radar Polarimetry, Ship detection, TerraSAR-X.

Armando Marino is with the ETH Zurich, Institute of Environmental Engineering, Zurich, Switzerland (e-mail: marino@ifu.baug.ethz.ch).

I. Introduction

The aim of the work described in this paper is the development of an innovative ship detector, based on Synthetic Aperture Radar (*SAR*) polarimetry and the methodology pioneered in [1], [2], [3], [4], namely *perturbation analysis*. Ship detection is a key topic for the surveillance of maritime areas largely due to the capability to acquire valuable images independent of solar illumination and (to some extent) weather conditions [5]. In the new procedure, targets are detected by exploiting the difference between the polarimetric characteristics of sea clutter and the targets of interest (e.g. ships, icebergs, etc).

In the literature, several works have described ship detection using radar polarimetry [6], [7], [8], [9], [10], [11] and they are based both on physical and statistical methodologies. The algorithm proposed in this paper is based on a physical rather than a statistical technique and it will be referred to as *Geometrical Perturbation-Polarimetric Notch Filter* (GP-PNF). Please note, the name Polarimetric Notch Filter was already introduced in the past by at least two more authors [12], [13], [14]. The algorithm proposed in this paper is based on a completely different methodology based on a Geometrical Perturbation analysis, as described in the following.

As for an ordinary notch filter, the algorithm rejects the selected target (in our case the sea) and detects anything different from it [15], [16], [17]. However, the original Notch Filter operates on the frequency domain (i.e. the Fourier transform of the signal in time), while the proposed Notch Filter is applied on a target polarization space (6 dimensional complex) where the partial targets lay.

In the following a very brief introduction to polarimetry is presented, focusing mainly on the mathematical tools exploited in the development of the detector. A single target is any target scattering an Electromagnetic (*EM*) wave having a fixed polarization in time/space [18], [19]. The latter can be characterized using a unique scattering (Sinclair) matrix:

$$[S] = \begin{bmatrix} HH & HV \\ VH & VV \end{bmatrix}, \tag{1}$$

or equivalently a scattering vector:

$$\underline{k} = \frac{1}{2} Trace\left([S]\Psi_2\right) = [k_1, k_2, k_3, k_4]^T, \tag{2}$$

where $Trace(.)$ is the sum of the diagonal elements of the matrix inside and Ψ_2 is a complete set of 2x2 basis matrices under a Hermitian inner product [19]. Finally, it is possible to define the scattering mechanism (*SM*) as a normalized vector $\underline{\omega} = \underline{k}/|\underline{k}|$.

Generally, the targets observed by a *SAR* system are not ideal *SM*, but a combination of different objects which we refer to as *partial* targets [20], [21]. In order to characterize a partial target a single scattering matrix $[S]$ is not sufficient, since it is a stochastic process and second order statistics are required. In this context, the target covariance matrix can be estimated:

$$[C] = \left\langle \underline{k}\, \underline{k}^{*T} \right\rangle, \tag{3}$$

where $\langle\,\rangle$ is the finite averaging operator. In the cases that medium where the electromagnetic wave propagates (i.e. air) is reciprocal and the sensor is monostatic (i.e. same transmitting and receiving antenna), the scattering vector in a generic basis is three dimensional complex and the covariance matrix is 3x3. In the literature, when $\underline{k}$ is expressed in the Pauli basis (i.e. $\underline{k} = \frac{1}{\sqrt{2}}[HH + VV, HH - VV, 2HV]^T$), the covariance matrix takes the name of *coherency matrix* $[T]$ [18], [19].

The methodology proposed in this paper takes advantage of the polarimetric coherence (i.e. normalized cross correlation). If two different *SM*, $\underline{\omega}_1$ and $\underline{\omega}_2$, are considered, the polarimetric coherence is [19]:

$$\gamma_p = \frac{\underline{\omega}_1^{*T}[C]\underline{\omega}_2}{\sqrt{(\underline{\omega}_1^{*T}[C]\underline{\omega}_1)\,(\underline{\omega}_2^{*T}[C]\underline{\omega}_2)}}. \tag{4}$$

II. Ship detection with SAR

One of the main features of ships in SAR images is a relatively large backscattering signal compared with the sea background. The actual intensity of a vessel is dependent on many factors as the size, material and generally the presence of metallic reflectors (trihedral and dihedral) [22]. This led to the idea of using the intensity contrast between ships and sea clutter as a feature to discriminate between them. Several methodologies were proposed [23], [9], [24], [25], [26], [27], [28], [29], [30], [31]. Most of these techniques set a statistical test between target and clutter background. When a likelihood ratio test is exploited the threshold is generally set following a Neyman-Pearson methodology [32], fixing the probability of detection or false alarm given the probability density functions (pdf) of clutter and target [23], [9], [32]. In case the distribution of the target is unknown the test can be set exploiting a parameterized pdf for the sea clutter and setting a constant false alarm [24], [28]. The latter is often referred as Constant False Alarm Rate (CFAR). Moreover, many algorithms try to estimate the sea pdf parameters locally, in order to take into account the sea variability. However, this generally leads to a large computational time [9].

A. Ship detection with Polarimetric SAR

Many authors have pointed out that SAR polarimetry may have a valuable contribution in improving ship detection [6], [33], [11], [8], [7], [30]. As a simple example, it can be observed that the simple use of the cross-polarised channel (HV) instead than the co-polarised ones (HH or VV) increases substantially the detection performance (for incidence angles smaller that around 50 degrees) [7]. This is because the sea is supposed to not have scattering contribution in the cross-polarised channel, therefore improving the Signal to Clutter Ratio (SCR). Some of the methodologies are statistical [9]. In these techniques, several polarimetric channels are considered as independent measurements of the same target [6], [8], [30]. From the analysis provided by [6]and shared by other authors [16], [34], it was shown that quad polarimetric modes provide the best detection performance, followed by the dual co-polarization combination HH and VV.

A second type of polarimetric ship detectors is based on physical scattering properties of targets and ships. Shirvany etal and Touzi etal [34], [7] exploited the difference in coherence (or degree of polarization) shown by ships and sea clutter, while Nunziata et al [33] uses the reflection symmetry properties showed by the sea but not vessels to perform discrimination. A different methodology exploits the differences in the polarimetric signature between the sea and targets [17], [35], [15], [16] of which more details will be provided in the following sections.

III. Perturbation analysis for polarimetric data

A. Partial target detector (PTD)

The detector developed in this paper takes advantage of the methodology pioneered in [36], [4], that allowed the detection of partial targets (PTD). A complete treatment of the PTD can be found in [3], [36]. The first step is to introduce a vector formalism where each partial target can be uniquely defined with *one* vector. A *feature partial scattering vector* is introduced:

$$\begin{aligned} \underline{t} =& Trace([C]\Psi_3) = [t_1, t_2, t_3, t_4, t_5, t_6]^T = \\ =& [\left\langle |k_1|^2 \right\rangle, \left\langle |k_2|^2 \right\rangle, \left\langle |k_3|^2 \right\rangle, \left\langle k_1^{*T} k_2 \right\rangle, \left\langle k_1^{*T} k_3 \right\rangle, \left\langle k_2^{*T} k_3 \right\rangle]^T, \end{aligned} \tag{5}$$

where Ψ_3 is a complete set of 3x3 basis matrices under a Hermitian inner product. $\underline{t}$ lies in a subset of $\mathbb{C}^6$ and it has the first three elements real positive and the second three complex, since it is extracted from a Hermitian matrix. The partial target to be detected can be represented with $\underline{t}_T$ and the perturbed one with $\underline{t}_P$. The perturbed version is obtained starting from $\underline{t}_T$, with a rotation in the subset of the physically feasible targets. A change of basis is performed which makes the target of interest lies only on 1 component: $\underline{t}_T = \sigma_T[1,0,0,0,0,0]^T$. In the following, the normalized versions of $\underline{t}_T$ and $\underline{t}_p$ will be exploited: $\hat{\underline{t}}_T = \frac{\underline{t}_T}{\|\underline{t}_T\|} = [1,0,0,0,0,0]^T$ and $\hat{\underline{t}}_p = \frac{\underline{t}_p}{\|\underline{t}_T\|} = [a,b,c,d,e,f]^T$.

For the sake of brevity, here, only the final expression of the PTD is presented. However, the reader is redirected to [36], [4] where the mathematical derivation is performed employing perturbation analysis:

$$\gamma_d = \frac{1}{\sqrt{1 + RedR\left(\dfrac{\underline{t}^{*T}\underline{t}}{|\underline{t}^{*T}\hat{\underline{t}}_T|^2} - 1\right)}}, \tag{6}$$

where *RedR* stands for Reduction Ratio and more details regarding this parameter will be provide in the following (e.g. section III.C). The detector is finalized setting a threshold on γ_d as:

$$H_0 : |\gamma_d(P_T, P_c)| \geq T \text{ and } H_1 : |\gamma_d(P_T, P_c)| < T, \tag{7}$$

where H_0 is the hypothesis for detection and H_1 for rejection. Details regarding the selection of the parameters *RedR* and *T* can be found in [3], [2], [36].

B. Geometrical Perturbation-Polarimetric Notch Filter (GP-PNF)

The application proposed in this work is the detection of targets in a background composed exclusively by locally homogeneous clutter, as the sea [15], [16]. To achieve this goal, the general methodology is modified in the form of a notch filter.

Locally, the sea clutter is polarimetricaly well characterized. For instance, a widely employed model is the Bragg scattering. However, the strategy followed in this paper consists in avoiding models or assumptions to characterize the sea scattering, with the aim of achieving a larger applicability of the algorithm. The idea behind the GP-PNF is to reject the sea return and extract the remaining features (in a similar way to a target decomposition [20] even though the output is different from ordinary decompositions).

In this way the detector will be focused not just on ships but also on icebergs (depending on the geographic location), buoys, fish farms or any other structure located over the sea. Following the new mathematical formulation, the *partial scattering vector* $\underline{t}$ of the sea clutter can be completely described by a vector in a six dimensional complex space $\hat{\underline{t}}_{sea} \in \mathbb{C}^6$. The most efficient way to obtain $\hat{\underline{t}}_{sea}$ is by extracting it from the data, since physical models are generally approximations and sometimes they need a priori information to be accurate (e.g. wind speed and direction).

At contrary than the PTD a target of interest cannot be represented by solely one vector $\underline{t}_T$, since ships comes with many different shapes and dimensions. Moreover, it was demonstrated that the orientation of ships plays a vital role in the estimation of its polarimetric signature. For this reason, a linear combination of vectors is exploited to represent the targets of interest. In particular, the subset of interest is the one orthogonal to the vector representing the sea and therefore 5 dimensional complex. Such a subset is represented with Ω_T, hence each target of interest will have a vector $\underline{t}_T \in \Omega_T$, with $\Omega_T \perp \Omega_{sea}$. In order to perform the perturbation analysis as for the PTD, a projection matrix (of rank 5) for the subset of interest has to be defined [37]. The projection matrix can be named $[Pr_T]$. In the basis where the normalized sea clutter represent one axis (i.e. $\underline{t}_{sea} = [1, 0, 0, 0, 0, 0]^T$), the projection matrix could simply be

$$[Pr_T] = \frac{1}{\sqrt{5}} diag(0, 1, 1, 1, 1, 1), \tag{8}$$

which is clearly a rank 5 matrix. Subsequently, the diagonal elements of $[Pr_T]$ are perturbed in order to obtain a subset slightly different from the previous one:

$$[Pr_P] = diag(a, b, c, d, e, f), \tag{9}$$

where $|a|^2 + |b|^2 + |c|^2 + |d|^2 + |e|^2 + |f|^2 = 1$. In actual fact, the addition of the a component (i.e. first component) allows for a no-null projection of the vectors on the sea subspace Ω_{sea}. In this paper, a priori information regarding the target to be detected (i.e. the specific vessel) are not exploited, for this reason each of the components of the vessel covariance matrix are considered equally important. This leads to the expressions $b = c = d = e = f$ and $|a| << |b|$. Any vector $\underline{b}_T \in \Omega_{sea}$ can be obtained with

$$[Pr_T]\underline{x} = \underline{b}_T, \tag{10}$$

where, $\underline{x} = [x_1, x_2, x_3, x_4, x_5, x_6]^T$ is a generic vector in the $\mathbb{C}^6$ subset of the physical feasible targets [36], [4]. With the same procedure the vector lying in Ω_T can be calculated:

$$[Pr_P]\underline{x} = \underline{b}_P. \tag{11}$$

As for the PTD, in order to perform the perturbation analysis the weighted inner product between the target to detect and its perturbed version has to be performed. The weighting matrix [P] is built exploiting a Gramm-Schmidt ortho-normalization where the first vector is chosen $\underline{u}_1 = \underline{\hat{t}}_{sea}$. The unitary vectors orthogonal to $\underline{\hat{t}}_{sea}$ are u_i with $i = 2, 3, 4, 5$. Therefore, $[P] = diag(|\underline{\hat{t}}_{sea}^{*T}\underline{t}|^2, |\underline{u}_2^{*T}\underline{t}|^2, |\underline{u}_3^{*T}\underline{t}|^2, |\underline{u}_4^{*T}\underline{t}|^2, |\underline{u}_5^{*T}\underline{t}|^2, |\underline{u}_6^{*T}\underline{t}|^2)$ or more compactly $[P] = diag(P_1, P_2, P, 3, P_4, P_5, P_6)$. The detector becomes:

$$\gamma_n = \frac{([Pr_T]\underline{x})^{*T}\,[P][Pr_P]\underline{x}}{\sqrt{\left(([Pr_T]\underline{x})^{*T}\,[P][Pr_T]\underline{x}\right)\left(([Pr_P]\underline{x})^{*T}\,[P][Pr_P]\underline{x}\right)}}. \tag{12}$$

After few passages, the following expression can be found:

$$\gamma_n = \frac{1}{\sqrt{1 + \frac{|a|^2}{|b|^2}\frac{|x_1|^2 P_1}{|x_2|^2 P_2 + |x_3|^2 P_3 + |x_4|^2 P_4 + |x_5|^2 P_5 + |x_6|^2 P_6}}}. \tag{13}$$

$\underline{x}$ can be any vector in the subset of the physical feasible targets. In particular, if a priori information are not available a fair solution is not to favor any component. The author leaves as future work the test of different weights for the components based on vessels a priori information. To summarize in this work, it is chosen:

$$\underline{x} = \frac{1}{\sqrt{6}}[1, 1, 1, 1, 1, 1]^T, \tag{14}$$

which makes the detector equal to

$$\gamma_n = \frac{1}{\sqrt{1 + \frac{|a|^2}{|b|^2}\frac{P_1}{P_2 + P_3 + P_4 + P_5 + P_6}}}. \tag{15}$$

In the basis considered, the power of the target of interest is $P_T = P_2 + P_3 + P_4 + P_5 + P_6$ and the sea clutter is $P_{sea} = P_1$. Substituting these values in (15), the detector becomes:

$$\gamma = \frac{1}{\sqrt{1 + \frac{|a|^2}{|b|^2}\frac{P_{sea}}{P_T}}} = \frac{1}{\sqrt{1 + RedR\frac{P_{sea}}{P_T}}}. \tag{16}$$

In terms of partial vectors the sea clutter power is

$$P_{sea} = |\underline{t}^{*T} \hat{\underline{t}}_{sea}|^2. \tag{17}$$

Please note, the squaring is necessary because $\hat{\underline{t}}_{sea}$ is a unitary vector. The total power is

$$P_{tot} = \underline{t}^{*T} \underline{t}. \tag{18}$$

Therefore, the power of the "non-sea" targets is

$$P_T = P_{tot} - P_{sea} = \underline{t}^{*T} \underline{t} - |\underline{t}^{*T} \hat{\underline{t}}_{sea}|^2. \tag{19}$$

The detector could be completed by setting a threshold *T* to γ:

$$\gamma = \frac{1}{\sqrt{1 + RedR \, \dfrac{|\underline{t}^{*T} \hat{\underline{t}}_{sea}|^2}{\underline{t}^{*T} \underline{t} - |\underline{t}^{*T} \hat{\underline{t}}_{sea}|^2}}} > T. \tag{20}$$

The previous detector γ is based on the same construction than the PTD, however, some further mathematical passage has to be performed in order to make it a notch filter. As explained in details in [36], the PTD has a decision rule based on a SCR between target and complemental space. However, in ship detection the amount of backscattering coming from the sea is function of the ocean's roughness, which is related to many factors as wind speed, currents, swells, etc [38], [39]. Therefore, the balance between sea and target defined as SCR can vary across the same scene. On the other hand, a notch filter should be independent of the magnitude of the component to be cut, but only dependent on the location of this component. In order to correct for this effects, the sea backscattering has to be neglected in the analysis. This is mathematically accomplished redefining the matrix [P] exploited to set the weights of the inner product. In particular, $\underline{u}_1 = \hat{\underline{t}}_{sea}$ the first element of the matrix [P] has to be set constant: $[P] = diag(c, |\underline{u}_2^{*T}\underline{t}|^2, |\underline{u}_3^{*T}\underline{t}|^2, |\underline{u}_4^{*T}\underline{t}|^2, |\underline{u}_5^{*T}\underline{t}|^2, |\underline{u}_6^{*T}\underline{t}|^2)$, with $c \in \mathbb{R}^+$. Following the same formulation proposed previously, the GP-PNF becomes:

$$\gamma_n = \frac{1}{\sqrt{1 + RedR\dfrac{c}{\underline{t}^{*T}\underline{t} - |\underline{t}^{*T}\hat{\underline{t}}_{sea}|^2}}} > T. \tag{21}$$

The constant c can be incorporated in the parameter RedR:

$$\gamma_n = \frac{1}{\sqrt{1 + \dfrac{RedR}{\underline{t}^{*T}\underline{t} - |\underline{t}^{*T}\hat{\underline{t}}_{sea}|^2}}} > T, \tag{22}$$

where the symbol *RedR* is formally kept for consistency with previous formulations. Next section is dedicated to the setting of the parameters *RedR* and *T*.

In equation 22, the total power minus the power of the sea $\underline{t}^{*T}\underline{t} - |\underline{t}^{*T}\hat{\underline{t}}_{sea}|^2$ represents the power of the target of interest (e.g. a vessel). When this is high the expression $\frac{1}{\underline{t}^{*T}\underline{t} - |\underline{t}^{*T}\hat{\underline{t}}_{sea}|^2}$ will be proximal to zero, therefore the denominator of γ_n will be proximal to 1. This returns a γ_n proximal to 1. On the other hand, if there is only sea, the fraction $\frac{1}{\underline{t}^{*T}\underline{t} - |\underline{t}^{*T}\hat{\underline{t}}_{sea}|^2}$ will be very high (going to infinity) and the denominator of γ_n will go to infinity as well. This will return a value of γ_n proximal to zero. The detector parameters RedR and T define the sensitivity of the detector.

Analyzing the final expression it is also possible to observe the (theoretical) algorithm independence on the sea backscattering. $\hat{\underline{t}}_{sea}$ appears only in the expression $\underline{t}^{*T}\underline{t} - |\underline{t}^{*T}\hat{\underline{t}}_{sea}|^2$, where the sea component is removed from the total return. Please note, the sea backscattering is not included in the constant RedR, since the latter is set once for all and has no relationship with the local sea backscattering.

To summarize, in the final expression of the GP-PNF, the detection is set based on the backscattering of targets after the contribution of the sea is removed. The similarity with a target decomposition is more evident, even though here the decomposed power is inserted in an expression that constrains it between 0 and 1.

C. Parameter setting

Aim of this section is to make the GP-PNF automatic, which requires an adaptive selection of the detector parameters.

Considering the GP-PNF has two independent parameters, the threshold *T* is chosen arbitrarily (e.g. $T = 0.98$) and the *RedR* (Reduction Ratio) is set locally. The *RedR* can be easily set based on the minimum target of interest P_T^{min} selected for a specific sensor, considering the expected backscattering of vessels. Even though the sea backscattering is removed, a reference state is needed to obtain the rejection of false alarms. The latter are due to a not perfectly homogeneous background or simply the speckle statistics of sea and noise. Therefore:

$$RedR = P_T^{min}\left(\frac{1}{T^2} - 1\right). \tag{23}$$

A more optimal setting can be accomplished knowing the probability density function (pdf) of the detector γ_n. Unfortunately, the analytical expression is not trivial and the author leaves its derivation as future work. In the next section, more details regarding this are provided performing Monte Carlo simulations. As a final remark, please note, setting a threshold on the minimum target to detect P_T^{min} the GP-PNF can take into account for some polarimetric heterogeneity. The higher is P_T^{min} the more heterogeneity is allowed.

Another point to take into account to make the algorithm automatic is that over a large scene the sea polarimetric behavior may change due to local incidence angle, currents, wind effects, etc. This effects are particularly visible in higher frequencies as X-band [40]. However, it can be seen that in a local averaging window the sea continues to behave in a relatively homogeneous way. Therefore, the selection of the Notch in the target polarimetric space (i.e. $\underline{\hat{t}}_{sea}$) has to be performed with local measurements.

In this paper a simple procedure is followed for two main reasons: firstly, it will show the algorithm capability in a more clear way without alterations consequence of intensive pre-processing (where we do not know if the performances are due to the GP-PNF or the pre-processing), and secondly, it makes the final algorithm particularly fast. However, in the future, more sophisticated methodologies will be investigated with expected increasing of performances. In details, a large moving window W_{tr} is employed to estimate $\underline{\hat{t}}_{sea}$ and inside this area a second smaller moving window w is exploited to calculate $\underline{t}$ (the details regarding the windows size are presented in the validation section, since they are depending to the sensor and target to be detected [9]). The presence of a ship in W_{tr} is averaged out resulting in a value of $\underline{\hat{t}}_{sea}$ different from the only sea case, but also different from the ship alone (or a part of the ship if this is bigger in size than w). A solution exploiting guard windows was attempted showing not evident improvements. This is mainly due to the fact that ships are not homogeneous targets and the target window w generally includes only a portion of the entire ship. For this reason, even in case of hardly corrupted $\underline{\hat{t}}_{sea}$ a portion of ship is expected to be polarimetricaly different from the entire ship plus sea. Finally, it is important to notice that even if the ship is extraordinarily homogeneous and bright and the signature in the training W_{tr} is exactly equal to the one of w, the detection will be triggered as soon as the target window w is centered to an area of sea just outside the target (in this case the ship will be interpreted as background and the sea as target). This means that the edges of the ship (point of discontinuity between sea and ship) will still be detected. A similar reasoning could be extended to large icebergs: the algorithms should be able to detect the edges. Additionally, the local heterogeneity on icebergs may trigger detection on the internal parts as well. However, this are just speculations and the author leaves the test as future work before to provide conclusive statements.

Beside this theoretical reasoning, in the simulation section the issue of estimating $\hat{\underline{t}}_{sea}$ is treated and we remind to the following sections for more details regarding this issue.

D. *Dual polarimetric GP-PNF*

In order to characterize uniquely a partial target quad polarimetric data are necessary. However, in some instances the coherent acquisition of four polarizations is not feasible and only two coherent acquisitions can be performed (dual polarimetric mode) [19], [18]. The aim of this section is the development of a version of the algorithm applicable to dual polarimetric data.

The use of dual polarimetric data may also be interesting because for some sensors they are available with higher resolution or swath cover. Clearly, reducing the number of images (observables) the performances of the final algorithm are expected to be lower. Another interesting point leading the author to particularize the detector for this acquisition mode is that the satellite TerraSAR-X is promising to have a significant contribution on ship detection due to its very high resolution achievable from space [40]. However, its quad-polarimetric mode is only experimental.

A dual polarimetric scattering vector can be introduced as $\underline{k}_d = [k_1, k_2]^T$, with k_1 and k_2 being complex numbers (for instance *HH* and *VV*). The covariance matrix can be estimated as:

$$[C_d] = \begin{bmatrix} \langle |k_1|^2 \rangle & \langle k_1^{*T} k_2 \rangle \\ \langle k_2^{*T} k_1 \rangle & \langle |k_2|^2 \rangle \end{bmatrix}. \tag{24}$$

Subsequently, a 3 dimensional partial feature vector can be built: $\underline{t}_d = Trace([C_d]\Psi_2) = \left[\langle|k_1|^2\rangle, \langle|k_2|^2\rangle, \langle k_1^{*T} k_2\rangle\right]^T$. Finally, the dual polarimetric GP-PNF is:

$$\gamma_{dn} = \frac{1}{\sqrt{1 + RedR \, \frac{1}{\underline{t_d}^{*T}\underline{t_d} - |\underline{t_d}^{*T}\hat{\underline{t}}_{dsea}|^2}}} > T, \tag{25}$$

where $\hat{\underline{t}}_{dsea}$ is the normalized dual polarimetric signature of the sea extracted with the large window W_{tr} and $\underline{t}_d$ is the partial vector extracted with the small window w.

In order to have an intuitive understanding of the differences between quad and dual data it has to be kept in mind that with dual-pol only a portion of the polarimetric space is observable. In order to obtain a detection, the projection of the target vector $\underline{t}_T$ in the observed dual-polarimetric space must be above the threshold. On the other hand, the null is selected considering exclusively the projection of the sea vector $\underline{t}_{sea}$ over the observed sub-space. Therefore, it is clear how a small projection in the dual-pol sub-space may lead to missed detection and false alarms respectively. Considering the sea has a behavior generally similar to a surface, the use of dual-pol HH/VV should to be theoretically advantageous compared to HH/HV.

As a summary of the processing performed, Figure 1 presents the flow chart of the algorithm. Very briefly, the polarimetric data (dual or quad pol) are processed in order to estimate the coherency matrices with two different moving windows (W_{tr} and w). Subsequently, the matrices are vectorized to obtain the $\underline{t}$ vectors. The latter accompanied be the detector parameters (e.g. $T = 0.98$ and $RedR = 2 * 10^{-3}$) are used to build the detector. The output of the algorithm is a detection mask.

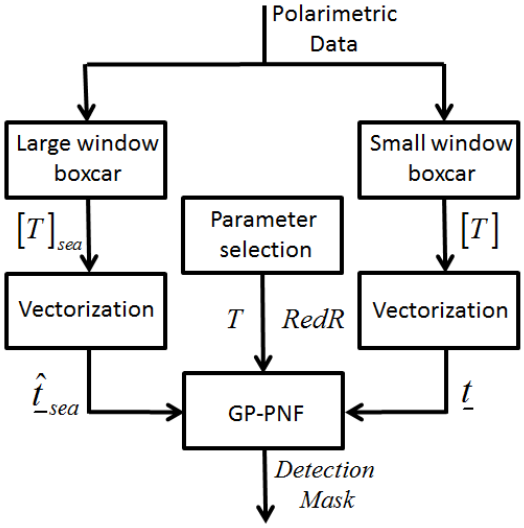

Fig. 1. Flow chart of the detector.

IV. Simulation

This section has the intention to test the statistical behavior of the GP-PNF. In particular, it will be shown that the GP-PNF is to some extent independent of: (*i*) the sea backscattering σ_{sea}; (*ii*) the specific sea polarimetric signature $\underline{t}_{sea}$. While in previous sections the asymptotic solution (eq. 22) shows the mathematical reasons for such independence, here these properties are tested from the statistical point of view. Ideally, the derivation of the probability density function (pdf) of γ_n would provide exact information. However, this is not trivial and the analytical solution may not exist. For this reason, this derivation is left as future work and here a simulation approach is adopted. The properties *i* and *ii* will be verified through a series of simulations based on the TerraSAR-X datasets.

A Monte Carlo simulation was designed, where σ_{sea} and $\underline{t}_{sea}$ can be arbitrarily modified. In the adopted statistical model, the sea clutter is generated by complex Gaussian random variables, where the asymptotic polarimetric signature is defined by a coherency matrix $[G_{sea}]$. The realization of a scattering vector $\underline{k}_{sea}$ for a generic pixel of sea can be estimated as

$$\underline{k}_{sea} = [G_{sea}]^{-\frac{1}{2}}\underline{u} \tag{26}$$

where $[G_{sea}]$ is the *generating* coherence matrix which represents the asymptotic coherence matrix. In this experiment $[G_{sea}]$ is extracted from the TerraSAR-X data selecting an area (200x200 pixels) with visual absence of vessels. The area exploited in this analysis is indicated by a white rectangle on the Pauli RGB image in Figure 9.b. $\underline{u} = [u_1, u_2, u_3]^T$ is a normalized three dimensional complex vector (i.e. $\underline{u} \in \mathbb{C}^3$) with components complex Gaussian random variables with zero mean (i.e. the real and imaginary part of each component is a zero mean Gaussian random variable with same standard deviation). For the sake of brevity, in this paper only quad polarimetric data were simulated, however the dual polarimetric case can be easily taken into account.

The simulated coherence matrix $[C_{sea}]$ (and subsequently the vector $\hat{\underline{t}}_{sea}$) is obtained by estimating the averaged outer product of independent realizations of $\underline{k}_{sea}$. If ${}^{i}\underline{k}_{sea}$ is a generic realization of $\underline{k}_{sea}$, the matrix $[C_{sea}]$ can be obtained as:

$$[C_{sea}] = \frac{1}{N}\sum_{i=1}^{N} {}^{i}\underline{k}_{sea}\ {}^{i}\underline{k}_{sea}^{*T} \tag{27}$$

The targets of interest are simulated extracting the coherence matrices corresponding to real targets in the TerraSAR-X dataset. The coherence matrices for three targets, two ships $[C_w]$, $[C_h]$ and a wind turbine $[C_t]$ were exploited. More details regarding these targets will be presented in the following sections. It is inevitable that, to some extent, a component from the sea surface will also be contained in $[C_w]$ and $[C_h]$, while $[C_t]$ does not represent the entire turbine, nevertheless these signatures represent some realistic matrices as they can be extracted from data. If $\sigma_{sea} = \|\underline{t}_{sea}\|$ and $\sigma_T = \|\underline{t}_T\|$ the Signal to Clutter Ratio (*SCR*) as interpreted by the detector can be calculated

$$SCR = \left(\frac{\sigma_T}{\sigma_{sea}}\right)^2. \tag{28}$$

Please note, the square is needed because the detector works with power of partial vectors. The target used presents the following values: $\|\underline{t}_w\| \approx 7.6$, $\|\underline{t}_h\| \approx 0.8$ and $\|\underline{t}_t\| \approx 19.4$.

A. *Independence with respect to* σ_{sea}

In this first simulation, the Null for the polarimetric signature of the sea $\hat{\underline{t}}_{sea}$ is simply extracted from the TerraSAR-X dataset. In this way, the simulation will be closer to a real scenario which does not consider any model assumption (except the Gaussian scattering). 500 simulations were performed with the *SCR* varying in the interval $[-20dB\ 20dB]$. Each simulation considers averaging a defined number of samples (N_w). The detection was run for each simulation and the probability of detection and false alarm was calculated as

$$P_D = \frac{N_D}{N},\ P_F = \frac{N_F}{N}. \tag{29}$$

where $N = 500$ is the total number of simulations (given a fixed *SCR*). N_D and N_F are respectively the number of detections and false alarms (given a fixed *SCR*). In other words, for each one of the 500 values of SCR the probabilities are calculated over 500 realizations each one generated with N_w samples averaged each other. The value used for RedR is the same used for real data: $RedR = 2 * 10^{-3}$ that returns a minimum target $P_T^{min} \approx 0.22$. This value was selected observing that all the targets of interest were showing much higher values. On the other hand, the value of N_w adopted in the simulation is 38, since in the real data the windows choice provides about 38 Equivalent Number of Looks (ENL).

Figure 2 shows the probability of detection P_D for the experiments. Only one of the three plots is presented since the P_D is steadily equal to one for all the three targets. Clearly, it

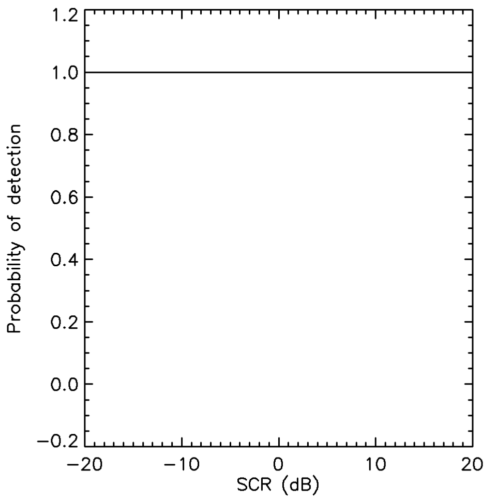

Fig. 2. Simulated probability of detection P_D for three targets varying the *SCR* in the interval $[-10dB\ 30dB]$ Averaging window: 170 samples. Number of simulations for each *SCR*: 500.

has to be considered that the accuracy is related to the quantization error of $1/2N = 10^{-3}$. The excellent results are consequence of the capability of the GP-PNF to delete the sea components before to set the threshold. If the final equation of the detector is analyzed (i.e. eq.22), the backscattering from $\underline{t}_{sea}$ does not appear. Even if the filter is not optimally set, and there is some spillage of sea power on the target subset, this will increase the value of $\underline{t}^{*T}\underline{t} - |\underline{t}^{*T}\hat{\underline{t}}_{sea}|^2$, since $|\underline{t}^{*T}\hat{\underline{t}}_{sea}|^2$ decreases, which increases the value of the detector γ_n (i.e. it provides a stronger detection).

P_F is presented in Figure 3. The horizontal axis represents the intensity of the sea clutter σ_{sea}. The trend of P_F has a very fast transition point σ_{sea}^c where the value pass from 0 to 1. This is because, in general, small errors in the statistical estimation of $[C_{sea}]$ are interpreted as a different target. When the intensity from the sea increases, a small estimation error can lead to a relatively high spilling of power in $\underline{t}^{*T}\underline{t} - |\underline{t}^{*T}\hat{\underline{t}}_{sea}|^2$, that may exceed P_T^{min}, triggering a detection. In conclusion, the increase of P_F is the result of errors in the estimation of the Null. In order to test this last idea, the same analysis was repeated utilizing a smaller and

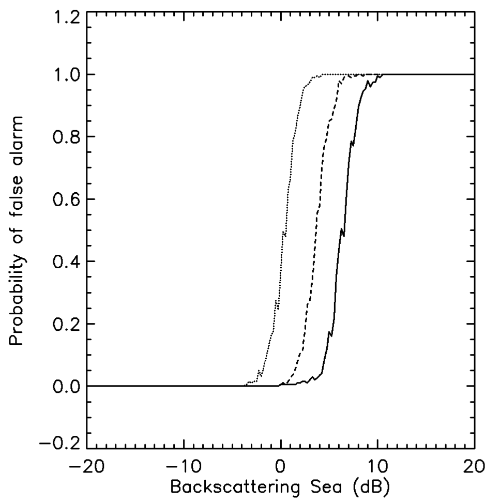

Fig. 3. Simulated probability of false alarm P_F for three target averaging windows varying the *SCR* in the interval $[-20dB\ \ 20dB]$. $RedR = 2 * 10^{-3}$. Solid line: 150 independent samples; Dashed line: 38 independent samples; Dotted line: 8 independent samples. Number of simulations for each *SCR*: 500.

bigger averaging window (respectively 8 and 150 independent samples). This test is also interesting in evaluating the sensitivity of the detector respect to the window size exploited. Reducing the averaging window, the transition point σ_{sea}^{c} moves towards the left (i.e. lower sea states). Interestingly, the sea is expected to have backscattering in VV always below $0dB$ [6] for common incidence angles (above 20 degrees). In other words, with 38 ENL the false alarm would be a problem only for unrealistically high values of σ_{sea}.

Observing Figure 3 it appears that for a window considering only 8 independent samples the false alarms are suppose to start appearing for value of $\|\underline{t}_{sea}\| \approx -2dB$ which are values that may be found in rough sea conditions. In case that an user would be interested in employing a very small target window the minimum target to detect should be increased in order to avoid false alarms (i.e. increasing RedR). Figure 4 shows the same simulation where now $RedR = 6 * 10^{-3}$, which corresponds to $P_T^{min} \approx 0.38$. With this value of RedR it is possible to recover the increase of false alarms showed by the smaller window of 8

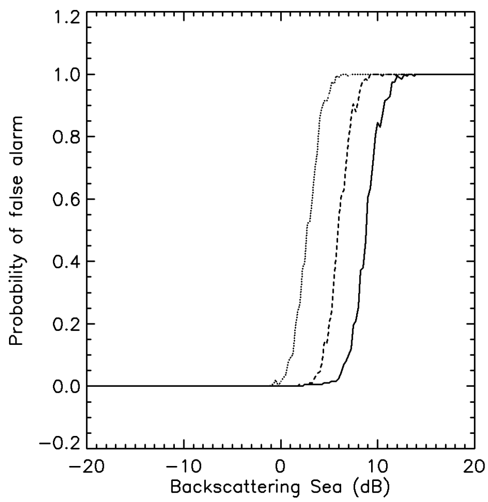

Fig. 4. Simulated probability of false alarm P_F for three target averaging windows varying the *SCR* in the interval $[-20dB\ 20dB]$. $RedR = 6 * 10^{-3}$ Solid line: 150 independent samples; Dashed line: 38 independent samples; Dotted line: 8 independent samples. Number of simulations for each *SCR*: 500.

independent samples. The latter test provides also information regarding the sensitivity of the detector with respect to the RedR parameter.

To conclude, the simulation showed that when the sea is very bright it will introduce false alarms, depending on the averaging window used. Fortunately, the values of sea backscattering required to trigger a false alarm are not expected in real data for incidence angles higher than 20 degrees.

B. Dependence on the target backscattering σ_T

The P_D estimated in the previous section is particularly good, showing perfect detection. However, in order to do not create false expectations, this section wants to locate the previous results in a larger context showing in which case the P_D can be smaller than 1.

In the selection of the detector parameters, the *RedR* is set with respect to a minimum target to detect (after the filtering). This means that the optimum performance, $P_D \approx 1$ can be obtained exclusively for $P_T \geq P_T^{min}$. Again, the presence of this lower boundary is not a

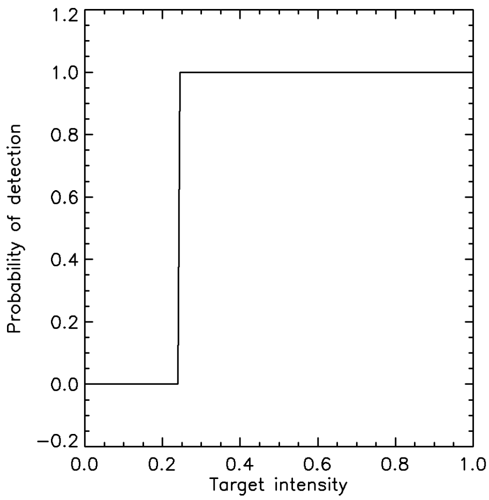

Fig. 5. Simulated probability of detection P_D for a vessel with intensity $||\underline{t}_w||$ varying in the interval $[0\ 1]$ (linear values). $RedR = 2 * 10^{-3}$ Averaging window: 38 samples. Number of simulations for each intensity: 500.

limitation, since it is needed to reject unwanted targets and estimation errors (i.e. due to the finite averaging). In order to test this property, Figure 5 shows the detection of the ship $\underline{t}_w$ varying its backscattering value (i.e. $||\underline{t}_w||$) between 0 and 1.

P_D goes from 0 when $||\underline{t}_w||$ is below P_T^{min} to 1 when it is above P_T^{min}. The crossing point is after 0.22, as set previously with the choice of the RedR. In details, the location of the crossing point is around 0.25 because the target $\underline{t}_w$ is not perfectly orthogonal to $\underline{t}_{sea}$ and the RedR is set considering the complementary space of $\underline{t}_{sea}$. However, the closeness of the crossing point to 0.22 is a good indicator that the signature of this vessel is quite orthogonal to the sea. Similar results were obtained repeating the same analysis with the other two targets (even closer to 0.22 for the turbine).

The same simulation is repeated in Figure 6 considering $RedR = 6 * 10^{-3}$ to cover the case of very small windows. Here, the crossing point is around 0.42, which is close to the theoretical value of 0.38.

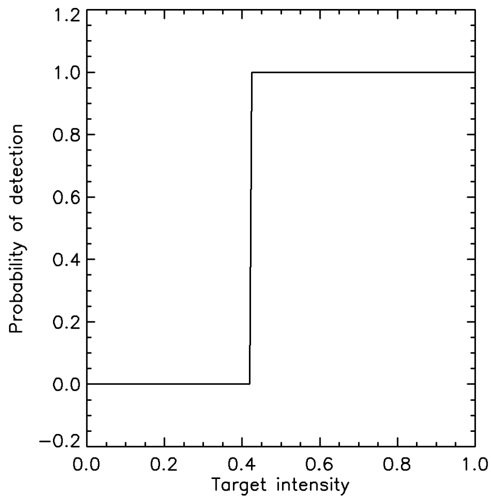

Fig. 6. Simulated probability of detection P_D for a vessel with intensity $\|\underline{t}_w\|$ varying in the interval $[0\ 1]$ (linear values). $RedR = 6 * 10^{-3}$. Averaging window: 38 samples. Number of simulations for each intensity: 500.

To conclude, if the target is very weak in the subset orthogonal to the vector representing the sea clutter, it will not be detected. This is useful to reject false alarms, but put a lower limit to the brightness of a detectable target.

C. Independence with respect to $\underline{t}_{sea}$

The independence of the specific sea polarimetric signature (i.e. $[C_{sea}]$) is investigated. In particular, the detector is supposed to have positive performance even if the polarimetric entropy [19], [20] of the sea H_{sea} (calculated as the entropy of the eigenvalues of $[C_{sea}]$) is equal to 1 (i.e. completely depolarized targets). This interesting result is consequence of the exploitation of the $\mathbb{C}^6$ space, where each partial target (including the one with entropy equal to 1) can be uniquely characterized.

A simulation was performed employing a completely depolarized sea clutter (i.e. $H_{sea} =$

1):

$$[C_{sea}] = [I], \tag{30}$$
$$\underline{k}_{sea} = \lambda[I]^{-\frac{1}{2}}\underline{u} = \lambda\underline{u}$$

where again, $\underline{u}$ is a 3 dimensional unitary complex Gaussian vector, $[I]$ is the identity matrix and λ is a real positive number. P_D and P_F are estimated with the same procedure illustrated previously.

The P_D plots are not presented, for the sake of brevity, since they are always equal to 1. This is because ships are not expected to have a polarimetric behavior equal to thermal noise. Theoretically, the only way to influence the detection through the selection of the Null is when the signature of the sea $\underline{t}_{sea}$ becomes equal to a class of targets (i.e. $\underline{t}_{sea} = \underline{t}_{T1}$). In this case, this and only this class of targets will be rejected from the detection mask, since it would be interpreted as sea. However, it would be unlikely that the sea surface acquires the same polarimetric scattering behavior of a complex structure as a vessel.

Figure 7 presents the probabilities of false alarm P_F for a sea clutter simulated as thermal noise. All the other parameters are the same employed in the previous simulation.

The probability of false alarm seems to have changed slightly compared to the previous simulation. In particular, the critical sea backscattering σ^c_{sea} seems to have moved leftward. This effect is again due to the quality of the estimation of the coherence matrix $[C_{sea}]$. In particular, the completely depolarized case represents one of the worst scenarios for extracting the second order statistics, since all the off-diagonal terms are theoretically equal to 0. A very large number of samples is necessary to estimate correctly these terms and estimation errors are more visible. Fortunately, the value of σ^c_{sea} for $ENL = 38$ is still higher than the expected upper boundary of sea backscattering (i.e. less than $0dB$), therefore P_F is supposed

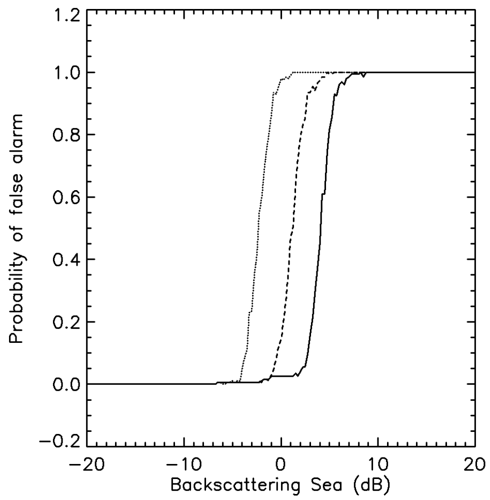

Fig. 7. Simulation of P_F for sea clutter completely depolarized (thermal noise), varying the intensity of the sea $\|\underline{t}_{sea}\|$ between $[-20dB\ 20dB]$. Solid line: 150 samples; Dashed line: 38 samples; Dashed line: 8 samples. Number of simulations for each intensity: 500.

to remain equal to zero in real data.

Summarizing, the algorithm is able to cope with different polarimetric signatures of the sea clutter, even though this may impact slightly on the false alarm rate. However, in the simulation performed the values at which the false alarms should appear are still unrealistic in real data especially because depolarized sea is mainly expected when the signal is very low (due to noise effects).

D. Errors in the selection of the Null

In this section, the issue of an highly heterogeneous sea is treated. As explained in the theoretical sections, $\underline{t}_{sea}$ can change in the same scene therefore the Null has to be set locally. However, algorithms for the extraction of $\underline{t}_{sea}$ may suffer of errors due to local heterogeneity or presence of a target in the averaging cell. Therefore, it is necessary to have some insight regarding the detector robustness with respect to these eventual errors.

In this simulation, $\underline{t}_{sea}$ was calculated as the superposition (in $\mathbb{C}^6$) of two contributions, one representing the target adopted as the Null (what we think is the sea) $\underline{t}_{null}$ and one orthogonal to this $\underline{t}_{\perp}$ (the error that we make):

$$[C_{sea}] = \sigma_{null}[C_{null}] + \sigma_{\perp}[C_{\perp}], \tag{31}$$

where

$$[C_{null}] \leftrightarrow \underline{t}_{null}, \; [C_{\perp}] \leftrightarrow \underline{t}_{\perp} \tag{32}$$

$$\underline{t}_{null} \perp \underline{t}_{\perp}$$

The amount of error on the estimation of $\underline{t}_{sea}$ is varied using a parameter defined as:

$$\rho_{sea} = \frac{||\underline{t}_{null}||}{||\underline{t}_{\perp}||}. \tag{33}$$

The signature of the sea $\underline{t}_{sea}$ is again extracted from the data in order to provide a more realistic scenario and $\rho_{sea} = 10$. The results of this simulation for P_D are not presented since they are again steadily equal to 1 (i.e. $P_D \approx 1$). The explanation is the same than the previous case.

A different course is suffered by P_F (depicted in Figure 8). The general trend (i.e. presence of a transition point σ_{sea}^c) resembles the previous scenario (Figure 3), however, now σ_{sea}^c has moved leftward (lower clutter power). This is because, the error component $\underline{t}_{\perp}$ lies in the subset of valuable targets and when the sea intensity is high, the projection over the error component can be large enough to trigger a detection. Fortunately, the value of σ_{sea}^c is still particularly high [6].

To conclude, the GP-PNF detector can have problems with false alarms if the sea background is not properly estimated. In a real scenario this translates in possible presence of false alarms when the background is particularly heterogeneous. This is for instance the case

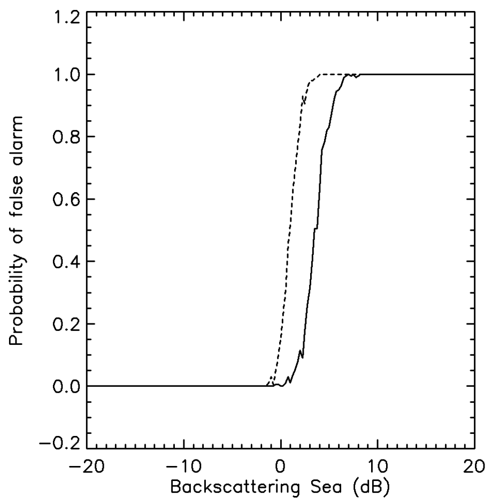

Fig. 8. Probability of false alarm P_F when the Null is not fixed exactly on the sea signature, varying $\|\underline{t}_{sea}\|$ in the interval $[-20dB\ 20dB]$. Solid line: no error $\rho = \infty$; Dashed line: 10% error $\rho = 10$. Number of simulations for each *SCR*: 500.

of sea ice clutter, where the GP-PNF in its current formulation would probably not be suited for ship/iceberg detection. Further work has to be carried out in this context.

V. VALIDATION WITH TERRASAR-X DATA

A. *TerraSAR-X data presentation*

TerraSAR-X represents an interesting scenario for ship detection, since it can acquire high resolution polarimetric data from space [40]. The datasets exploited in this validation considers quad polarimetry from DLR's Dual Receive Antenna (*DRA*) campaign in 2010. Unfortunately, the quad polarimetric mode of TerraSAR-X is only experimental and this typology of data are not ordinarily acquired. Nevertheless, using quad polarimetric data, it is possible to compare the detection performance between quad and dual modes. The two datasets cover the off-shore area north of Gröningen (Holland) and the harbor area of Barcelona (Spain). The resolution of the data is $1.18m$ in slant range and $6.6m$ in azimuth, while the sampling is $0.91m$ in range (equivalent to $1.48m$ in ground range) and $2.39m$ in azimuth.

The North Sea data were acquired the 23^{th} April and 12^{th} April 2010 with an incidence angle of 28 degrees. The area is of particular interest for the algorithm validation, since in the middle of the acquisition area there is the *Alpha Venta* wind farm. This is composed of 13 wind turbines and one substation (umspannwerk) [41]. A schematic illustrating the location of the wind turbines is showed in Figure 9.a. The Barcelona dataset considered in this paper is composed of 2 acquisitions on the same days: 23^{rd} April and 12^{th} of April 2010. The central incidence angle for both the acquisitions is 33.8 degrees.

In this test, an initial multi-look of 3x5 (range x azimuth) is performed to make the pixel more squared on the ground. Subsequently the target moving window (before defined as w) is 5x5. Considering the large over-sampling, the *ENL* is lower than the number of samples, ending up with about 38 independent looks (this is the reason why this value was used in the simulation). Considering the dimensions of the target of interest, this arrangement in window size was revealing the best. However, in case that the detection is focused on very small vessels, less pixels could be used. On the data available, using less pixels was still returning good detection capabilities however, the simulations performed in the previous section were suggesting possible problems with false alarms using small windows. For this reason, results with small windows are not presented here and in the future better ground truth will be employed to validate such window configuration. The big averaging window W_{tr} exploited to extract the value of $\hat{\underline{t}}_{sea}$ is 50 x 50 after the multi-look ending up with $ENL \approx 10,000$ (the area covered is about $\sim 600mx600m$). The parameters used for the detection are the same evaluated in the simulation section: i.e. $T = 0.98$ and $RedR = 2*10^{-3}$, which returns a minimum target $P_T^{min} \approx 0.22$.

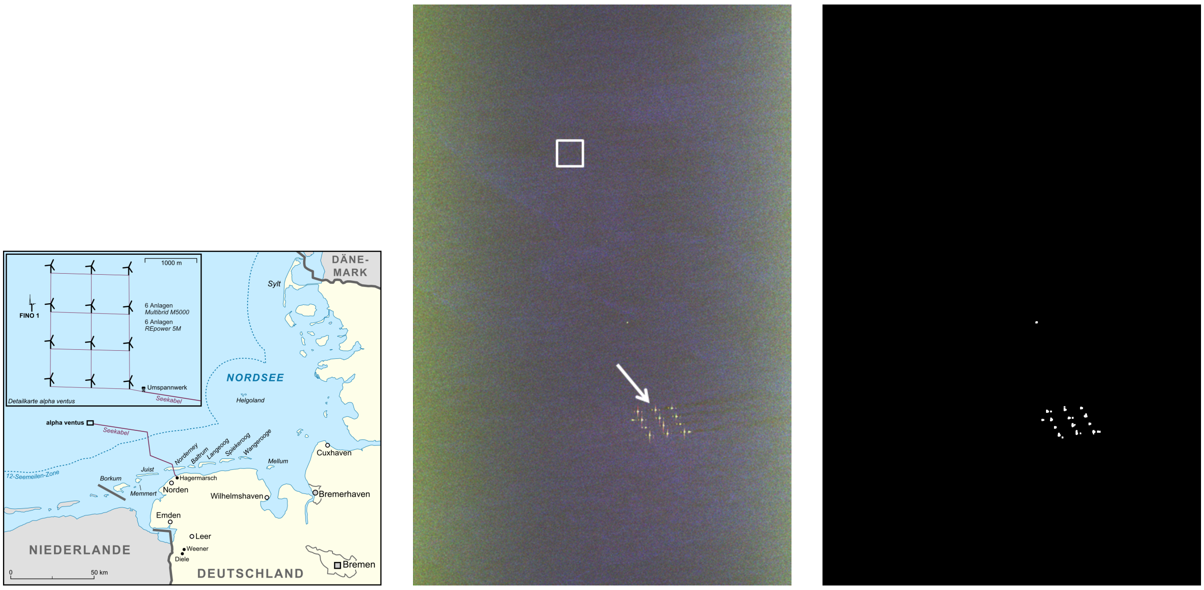

(a) Alpha Venta (b) *RGB* Pauli (c) Quad GP-PNF

Fig. 9. TerraSAR-X Quad polarimetric date over Alpha Venta wind farm (North Sea, 23^{th} April 2010): (a) Alpha Venta illustration (b) *RGB* Pauli composite image (c) GP-PNF detection with quad-pol.

B. Validation results: North Sea

The Pauli *RGB* image of the area is illustrated in Figure 9.b.

The wind turbines are visible in the *RGB* image where the range direction is horizontal (left to right). The arrow indicates the turbine that was used to extract the signature for the previous simulations. No special rule was used to choose that specific turbine, since the signatures are relatively similar.

The polarimetric signature of the sea appears slowly to vary along the range direction due to incidence angle and noise effects for HV. For this reason, the dataset is valuable to evaluate the robustness of the proposed adaptive algorithm with respect to changes in the sea polarimetric signature $\underline{\hat{t}}_{sea}$. Unfortunately, meteorological information at the time of the acquisition are not available, however, an easy way to have an idea about the difficulty of the detection exercise is to evaluate the maximum value of the sea backscattering in an averaging window. In the present dataset the maximum value of the sea intensity in the VV polarization is around 0.3, showing moderate wind conditions.

Figure 9.c depicts the GP-PNF mask exploiting quad polarimetric data. The mask is obtained setting to 0 (i.e. black) all the pixels where $\gamma_n < T$ and 1 where $\gamma_n > T$. Moreover, merely for visualization purposes, every time that a point is detected it is expanded in the mask to a squared area of 20x20 pixels. Again this is only to allow a good visualization of the mask and an automatic algorithm will not need to perform this enlargement. This is also useful to have a visual assessment of false alarms since even a single-pixel false alarm would have a large visualized area in the mask.

The mask shows that the 13 wind turbines and substation (umspannwerk) are correctly detected. Moreover, there is another target that is detected. Unfortunately, ground truths are not available to confirm that it is a vessel, however its backscattering is particularly high making us believe it is a genuine detection. An interesting point is that the adaptive selection of the null is able to follow the changes of the sea surface even though $\underline{\hat{t}}_{sea}$ appears to change from near to far range. In order to test the dual polarimetric version of the detector, Figure 10.a and Figure 10.b present the detection mask of the GP-PNF when the dual polarimetric HH/VV and HH/HV modes are exploited.

Again all the turbines, the substation and the unknown-vessel are detected. This is because these targets present a large backscattering in a wide portion of the target space, therefore they will have a significant projection also in the subset observable by the dual-pol mode.

The detection over the second dataset in the North Sea are presented in Figure 11. The maximum intensity of the sea in the VV polarization is around 0.25, showing a moderate sea state.

As for the previous case, all the wind turbines and substation are detected with all the

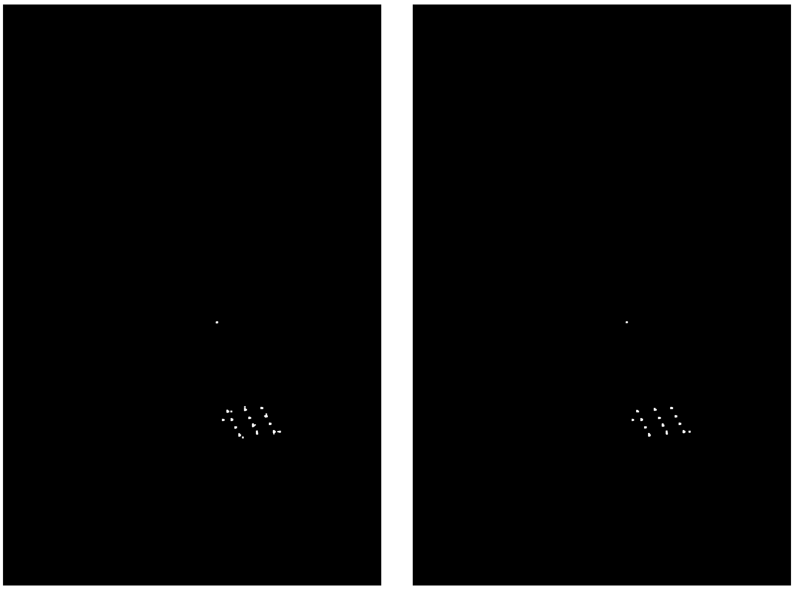

(a) Dual-pol HH/VV GP-PNF (b) Dual-pol HH/HV GP-PNF

Fig. 10. TerraSAR-X detection over Alpha Venta wind farm (North Sea, 23^{th} April 2010): (a) Detection with dual pol HH/VV GP-PNF (b) Detection with dual pol HH/HV GP-PNF.

(a) RGB Pauli (b) Quad-pol GP-PNF (c) Dual-pol HH/VV GP-PNF (d) Dual-pol HH/HV GP-PNF

Fig. 11. TerraSAR-X detection over Alpha Venta wind farm (North Sea, 12^{th} April 2010): (a) RGB Pauli composite image (b) Detection with GP-PNF quad-pol (c) Detection with GP-PNF dual-pol HH/VV (d) Detection with GP-PNF dual-pol HH/HV.

modes. Additionally, there are two bright areas in the images that are detected. The one in the upper part of the image is clearly a vessel since its wake is visible. The other, just north of the wind farm, is particularly bright and it is quite unlikely to be a false alarm (it is probably a supervision boat). Unfortunately, ground truths are not available to confirm this last theory.

Regarding the analysis of false positive, all the detection performed in these two experiments do not present any false alarm (as long as the three very bright pixels are genuine vessels).

C. Validation results: Barcelona

The second test considers the two Barcelona's datasets. Firstly, the 23^{rd} of April is analyzed. Figure 12.a shows the *RGB* Pauli composite image. The sea return seems particularly low, due to the low wind conditions. The most of the sea region is black in the *RGB*. In the upper right corner, three bright points are visible. One of them is clearly a vessel due to the wake. Moreover in the lower left part of the image, many green spots appear randomly distributed. We believe that the most of those green points are due to image artefact particularly visible when the sea backscattering is low. However, in the same location where the green spots appear there are several fish farms. Unfortunately, it was not possible to find any credited photo or nautical chart of the area to confirm that they are not artefact.

The arrows indicates two of the target signatures used previously in the simulation session. Specifically, $\underline{t}_w$ is the vessel with the wake, while $\underline{t}_h$ is the upper vessel close to the harbor entrance. The white rectangle indicates an area that in the following will be used to have a zoom trying to spot small targets (i.e. using a smaller target window, as described in the following).

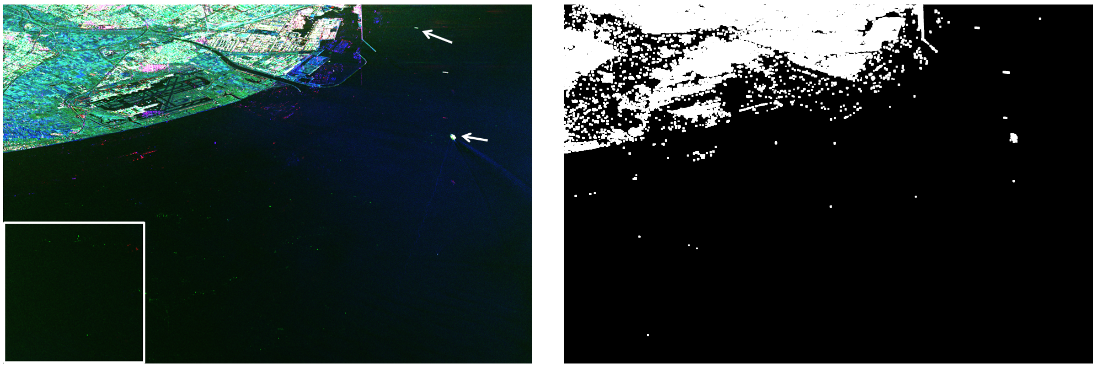

(a) RGB Pauli (b) GP-PNF quad-pol

Fig. 12. TerraSAR-X Quad pol date over Barcelona harbor (Mediterranean, 23^{rd} of April 2010): (a) RGB Pauli composite image (b) Detection with GP-PNF quad-pol.

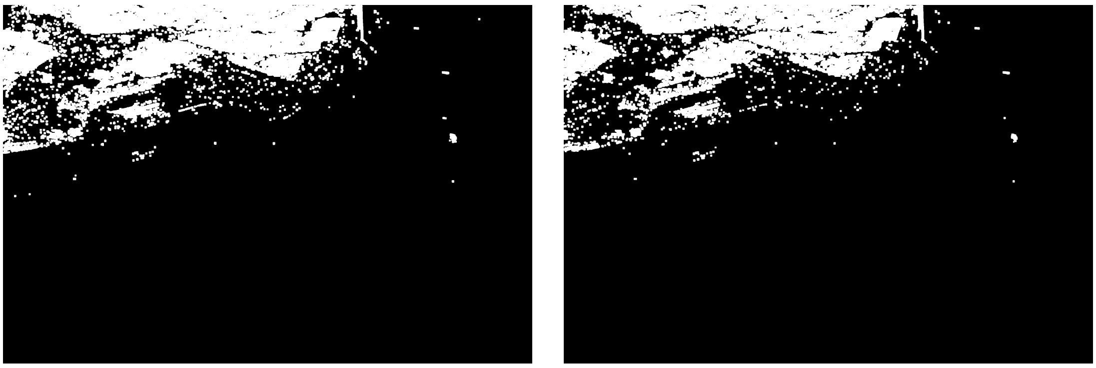

(a) Dual-pol HH/VV GP-PNF (b) Dual-pol HH/HV GP-PNF

Fig. 13. TerraSAR-X quad-pol date over Barcelona harbor (Mediterranean, 23^{rd} of April 2010): (a) Detection with GP-PNF dual-pol HH/VV (b) Detection with GP-PNF dual-pol HH/HV.

The detection masks with quad pol is presented in Figure 12, while Figure 13 shows the detection with dual-pol data.

All the versions of the algorithms are able to detect the three ships. However, there are two bright red points (very likely ghost of two of the vessels) that cannot be detected with the HH/HV mode. This is because the scattering is mainly in HH-VV that is not completely observed by the HH/HV mode. Clearly, they are not genuine detection (and they can be corrected checking for the position of the nearby bright vessels), but in this experiment they are usefull to understand in which situation the HH/HV mode would fail. The green points

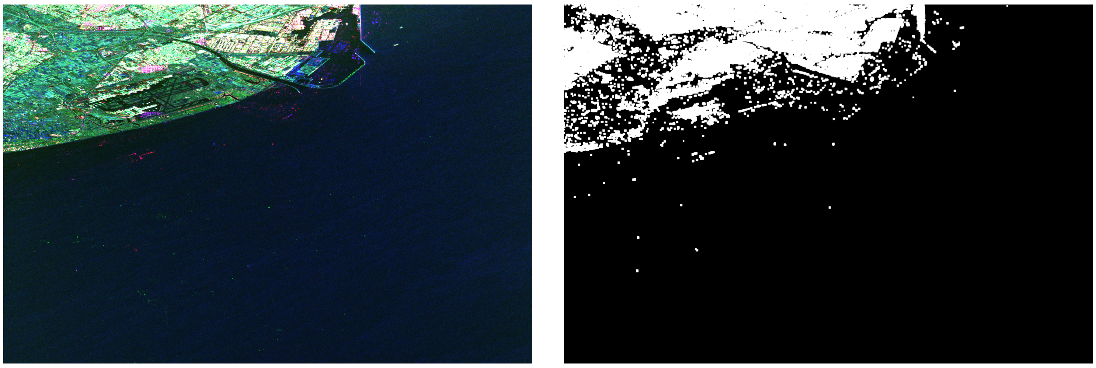

(a) RGB Pauli (b) GP-PNF quad-pol

Fig. 14. TerraSAR-X Quad pol date over Barcelona harbor (Mediterranean, 12^{rd} of April 2010): (a) RGB Pauli composite image (b) Detection with GP-PNF quad-pol.

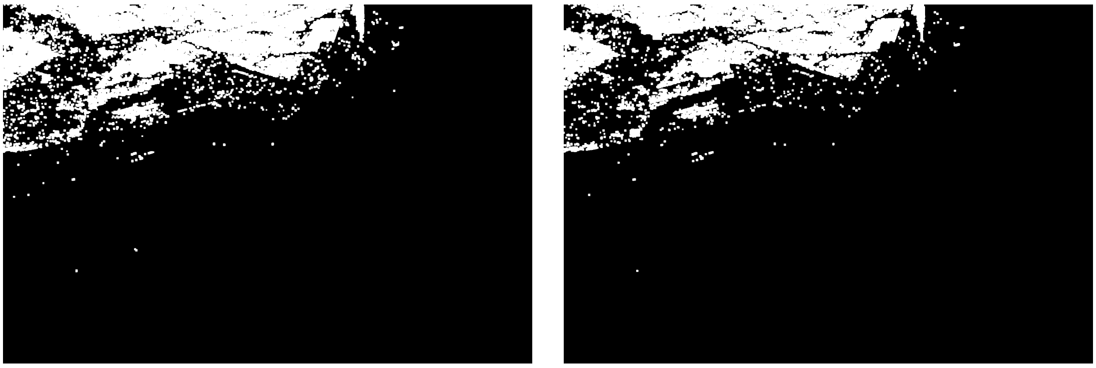

(a) Dual-pol HH/VV GP-PNF (b) Dual-pol HH/HV GP-PNF

Fig. 15. TerraSAR-X quad-pol date over Barcelona harbor (Mediterranean, 12^{rd} of April 2010): (a) Detection with GP-PNF dual-pol HH/VV (b) Detection with GP-PNF dual-pol HH/HV.

in the *RGB* image are only partially detected (more details will be provided in the following section).

The second dataset was acquired the 12^{rd} of April 2010. The images for the two dates are roughly co-registered over the land area with a simple correlation algorithm. Figure 14 shows the RGB Pauli with the GP-PNF quad-pol mask, while Figure 15 depicts the dual-pol GP-PNF detectors. Here, two vessels are visible close to the harbor and it is possible to detect them with all the modes.

In order to have an insight about the green spots in the left lower corner Figure 16 presents a crop of the image with Pauli RGB and quad-pol GP-PNF masks for both the acquisitions. Considering the targets are expected to be smaller the target window is modified from $[5, 5]$ to $[3, 3]$. The latter correspond to an $ENL \approx 8$. The previous section was showing that when the sea has a backscattering higher than 0.8, $ENL = 8$ may introduce some false alarms. Fortunately, this is not the case in this dataset, but care has to be put when other datasets are considered. Finally, the detected points are not expanded as for the previous section, since each of the detection should be more visible in this zoomed image.

Analyzing the two Pauli RGB images it can be observed that the most of the green spots are located in exactly the same areas. The fact that the point did not move during the 11 days is a hint that they represent either ambiguities from the nearby city or anchored targets (as fish farms). In particular, the Y shaped red spot is an azimuth ambiguity. As a general idea, if the GP-PNF is set to detect small targets it detects also the most of the ambiguities since they represent heterogeneities over homogeneous background. A pre-processing algorithm should be exploited in such cases. The detection masks, shows that in the two acquisitions the same targets are detect (except for a point in the middle of the image that we presume is a small vessel judging from the polarimetric signature in the RGB image). This is an interesting result since it shows that the algorithm is able to detect the same targets in two different sea conditions (i.e. it evaluates only the power coming from the targets).

The final experiment tests the dual-pol detectors over the weak targets. The detection masks of the GP-PNF applied with HH/VV and HH/HV are presented in Figure 17. Comparing the results for dual- and quad-pol GP-PNF, the latter detects more points. Although, all the detections correspond to bright points in the RGB image, ground truths of the area are not available and it is not possible to know whether these points are genuine detections or false alarms (please note, in this context ambiguities can be considered as true positives even though they would be removed in an operative stage). Nevertheless, it is possible to see a general higher detection capability of the quad-pol GP-PNF. Moreover, it is hard to decide which dual-pol mode performs better, since both have a comparable number of detected points.

After this second analysis, some conclusions could be drawn regarding the importance of the cross polarization for detection of man made targets over sea clutter with TerraSAR-X. When the GP-PNF was focused on detection of medium/large vessels all the modes had similar performance, detecting all the turbines and points that can be visually interpreted as vessels in all the North Sea and Barcelona datasets. On the other hand, when the detection was focused on smaller vessels (and what was supposed to be fish farms), the quad-pol showed better performance compared to the dual-pol modes. Regarding, the best mode between HH/VV and HH/HV, it was not possible to draw conclusions with the available datasets due to the lack of accurate ground truth. However, considering the typology of scattering expected by vessels and the fact that the sea can be very well characterized by using the two co-polarizations, the HH/VV mode should be advantageous compared to HH/HV. Further work will be carried out on this issue.

VI. Conclusion

In this paper an adaptive Geometrical Perturbation-Polarimetric Notch Filter (GP-PNF) for detection of maritime features (ship, buoys, icebergs, etc) was proposed. The GP-PNF detects the features which are polarimetricaly different from a local homogeneous clutter background as it is the sea. The proposed algorithm is adaptive and it is able to select automatically the polarimetric signature of the sea (used to set the Notch) locally. The detector is initially developed for quad polarimetric data, since they assure the uniqueness of the target characterization, however, a dual polarimetric version is proposed too, in order to take into account the situations when quad pol data can not be acquired.

The algorithm was tested on 4 quad polarimetric TerraSAR-X datasets acquired during the Dual Receiver Campaign in 2010 on areas including a wind farm (Alpha Venta) in the North Sea and the harbor of Barcelona. The detection masks are in agreement with available ground truth and expected targets in the area.

The comparison between dual and quad polarimetric GP-PNF showed very similar results when the GP-PNF was focused on medium/large vessels. However, when tested with small vessels (and fish farms) the quad-pol GP-PNF was able to detect more targets. But unfortunately accurate ground truth are not available to confirm that these are genuine detections. For the same reason was not possible to identify which mode between HH/VV and HH/HV performed better. However, considering the expected scattering from vessels and sea the HH/VV should be able to characterize better either sea and vessels. For this reason, HH/VV should be (at least theoretically) preferred to HH/HV.

The third part of the paper was dedicated to the test of the GP-PNF with Monte Carlo simulations. Specifically, two points were under analysis: the independence of the GP-PNF with respect to (*i*) the sea backscattering σ_{sea} and (*ii*) the specific sea polarimetric signature $\underline{t}_{sea}$. The simulations showed notable performance with theoretical probability of detection $P_D \approx 1$ and probability of false alarm $P_F \approx 0$. Moreover, further analysis were performed in order to understand in which circumstances the detector performance can reduce. Specifically, P_D is lower than 1 when the targets have a backscattering lower than a fixed minimum (which can be chosen) and P_F is higher than 0 when there are errors in the estimation of the sea signature (the value chosen for the Null).

As a future work, the probability density function (pdf) of the detector will be investigated in order to perform an analytical assessment of the detector performance. Moreover, further validation with a large variety of sea states will be attempted, in order to understand the limits of the GP-PNF. With the same dataset, the best dual-pol mode between HH/VV and HH/HV will be investigated as well.

VII. Acknowledgments

This work was partially supported by the ESA programme, ”VAE actions to integrate new developments into EO services”, ESRIN contract number 22568/09/I-EC. Also the author would like to thank eOsphere to have partially funded the work presented in this paper. TerraSAR-X data were provided by DLR in the framework of the AO for Dual Receive Antenna (DRA) 2010 campaign.

References

[1] A. Marino, S. R. Cloude, and I. H. Woodhouse, “A polarimetric target detector using the Huynen Fork,” *IEEE Trans. on Geos. & Rem. Sens.*, vol. 48, pp. 2357–2366, 2010.

[2] A. Marino, S. R. Cloude, and I. H. Woodhouse, “Detecting depolarizing targets with satellite data: a new geometrical perturbation filter,” *IEEE Int. Geos. & Rem. Sens. Symp. IGARSS*, 2010.

[3] A. Marino and S. R. Cloude, “Detecting depolarizing targets using a new geometrical perturbation filter,” *Proc. on EUSAR’10, Achen, Germany, June*, 2010.

[4] A. Marino, *A New Target Detector Based on Geometrical Perturbation Filters for Polarimetric Synthetic Aperture Radar (POL-SAR)*, Springer-Verlag, 2012.

[5] V. Barele and M. Gade, *Remote Sensing of the European Seas*, Springer, 2008.

[6] C. Liu, P. W. Vachon, and G. W. Geling, “Improved ship detection using polarimetric SAR data,,” *IGARSS Geoscience and Remote Sensing Symposium*, vol. 3, pp. 1800–1803,, 2004.

[7] R. Touzi, “On the use of polarimetric SAR data for ship detection,” *IGARSS Geoscience and Remote Sensing Symposium*, vol. 2, pp. 812–814, 1999.

[8] R. Ringrose and N. Harris, “Ship Detection Using Polarimetric SAR Data,” *SAR Workshop: CEOS Committee on Earth Observation Satellites*, 2000.

[9] D. J. Crisp, "The State-of-the-Art in ship detection in Synthetic Aperture Radar imagery," *Australiane Government Department of Defence*, 2004.

[10] D.J. Crisp and T. Keevers, "Comparison of ship detectors for polarimetric sar imagery," *OCEANS 2010 IEEE - Sydney*, pp. 1–8, 2010.

[11] F. Nunziata, A. Montuori, and M. Migliaccio, "Dual-polarized cosmo skymed sar data to observe metallic targets at sea," *IGARSS , Geoscience and Remote Sensing IEEE International Symposium*, pp. 2270–2273, 2011.

[12] A. J. Poelman, "Virtual polarization adaptation. a method of increasing the detection capability of a radar system through polarization vector processing," *Proceedings IEE*, vol. 128, No. 5,, pp. 261–270, 1981.

[13] A. J. Poelman and K. J. Hilgers, "The effectiveness of multi-notch logic product polarization filters in radar for countering rain clutter," *Kluwer Academic Publishers*, 1992.

[14] K. Suwa, K. Yamamoto, C. Nonaka, A. Imamura, and T. Kirimoto, "A target detection algorithm using polarimetric notch filter," *Electronics and Communications in Japan (Part I: Communications)*, vol. 88, Issue 3, pp. 33–43, 2005.

[15] A. Marino, N. Walker, and I. H. Woodhouse, "Ship detection using SAR polarimetry. the development of a new algorithm designed to exploit new satellite SAR capabilities for maritime surveillance," *Proceedings on SEASAR, Frascati, Italy, January*, 2010.

[16] A. Marino, N. Walker, and I. H. Woodhouse, "Ship detection with SAR data using a notch filter based on perturbation analysis," *Proceedings on IGARSS, Honolulu, Hawaii, July*, 2010.

[17] A. Marino and N. Walker, "Ship detection with quad polarimetric terrasar-x data: an adaptive notch filter," *Proc. on IGARSS11*, 2011.

[18] J. S. Lee and E. Pottier, *Polarimetric radar imaging: from basics to applications*, CRC Press, Taylor & Francis Group, 2009.

[19] S. R. Cloude, *Polarisation: Applications in Remote Sensing*, Oxford University Press, 2009.

[20] S. R. Cloude and E. Pottier, "A review of target decomposition theorems in radar polarimetry.," *IEEE Transaction on Geoscience and Remote Sensing*, vol. 34, pp. 498–518, 1996.

[21] G. A. Deschamps and P. Edward, "Poincare sphere representation of partially polarized fields," *IEEE Transaction on Antennas and Propagation.*, vol. 21, pp. 474–478, 1973.

[22] G. Margarit, J.J. Mallorquí, J. Fortuny-Guasch, and C. López-Martínez, "Exploitation of ship scattering in polarimetric sar for an improved classification under high clutter conditions," *IEEE Transactions on Geoscience and Remote Sensing*, vol. 47, 2009.

[23] M. Brizi, P. Lombardo, and D. Pastina, "Exploiting the shadow information to increase the target detection performance in sar images.," *International Conference on Radar Systems, RADAR99*, 1999.

[24] K. Eldhuset, "An automatic ship and ship wake detection system for spaceborne sar images in coastal regions.," *IEEE Transactions on Geoscience and Remote Sensing*, vol. 34, pp. 1010 – 1019, 1996.

[25] K. Ouchi, S. Tamaki, H. Yaguchi, and M. Iehara, "Ship detection based on coherence images derived from cross correlation of multilook sar images," *IEEE Geoscience and Remote Sensing Letters*, vol. 1, 2004.

[26] A.J. Rye, F.G. Sawyer, and R. Sothinathan, "A workstation for the fast detection of ships," *Proceeding on IGARSS90*, vol. 3, 1990.

[27] M. Sciotti and P. Lombardo, "Ship detection in sar images: a segmentation-based approach.," *Proceedings of the 2001 IEEE Radar Conference*, 2001.

[28] P. W Vachon, "Ship detection in synthetic aperture radar imagery.," *Proceedings OceanSAR, St. John s, NL, Canada*, 2006.

[29] C.C. Wackerman, K.S. Friedman, W.G. Pichel, P. Clemente-Colon, and X. Li, "Automatic detection of ships in radarsat-1 sar imagery," *Canadian Journal of Remote Sensing*, vol. 27, 2001.

[30] M. Yeremy, G. Geling, M. Rey, B. Plache, and M. Henschel, "Results from the crusade ship detection trial: polarimetric sar.," *Proceeding on IGARSS 2002*, 2002.

[31] C. Brekke, S.N. Anfinsen, and Y. Larsen, "Subband extraction strategies in ship detection with the subaperture cross-correlation magnitude," *IEEE Geoscience and Remote Sensing Letters*, 2012.

[32] S. M. Kay, *Fundamentals of Statistical Signal Processing*, Prentice Hall, 1993.

[33] F. Nunziata, M. Migliaccio, and C.E. Brown, "Reflection symmetry for polarimetric observation of man-made metallic targets at sea," *IEEE Journal of Oceanic Engineering,*, vol. 37, 3, pp. 384–394, 2012.

[34] R. Shirvany, M. Chabert, and J.-Y. Tourneret, "Ship and oil-spill detection using the degree of polarization in linear and hybrid/compact dual-pol sar," *IEEE Journal of Selected Topics in Applied Earth Observations and Remote Sensing*, 2012.

[35] A. Marino and N. Walker, "Ship detection in variable sea states and depolarised sea clutter: a polarimetric notch filter," *Proceeding on POLinSAR*, 2011.

[36] A. Marino, S. R. Cloude, and I. H. Woodhouse, "Detecting depolarized targets using a new geometrical perturbation filter," *IEEE Transaction on Geoscience and Remote Sensing*, vol. In press, 2012.

[37] G. Strang, *Linear Algebra and its Applications*, Thomson Learning, 1988.

[38] C. Elachi and J. van Zyl, *Introduction To The Physics and Techniques of Remote Sensing*, John Wiley and Sons, 2006.

[39] F. T. Ulaby, Moore R. K., and Fung A. K., *Microwave Remote Sensing Volume 3*, The Arthec House, 1986.

[40] S. Suchandt, H. Runge, and U. Steinbrecher, "Ship detection and measurement using the TerraSAR-X dual-receive antenna mode," *IEEE International Geoscience and Remote Sensing Symposium (IGARSS)*, pp. 2860 – 2863, 2010.

[41] "http://www.alpha-ventus.de/index.php?id=80," .

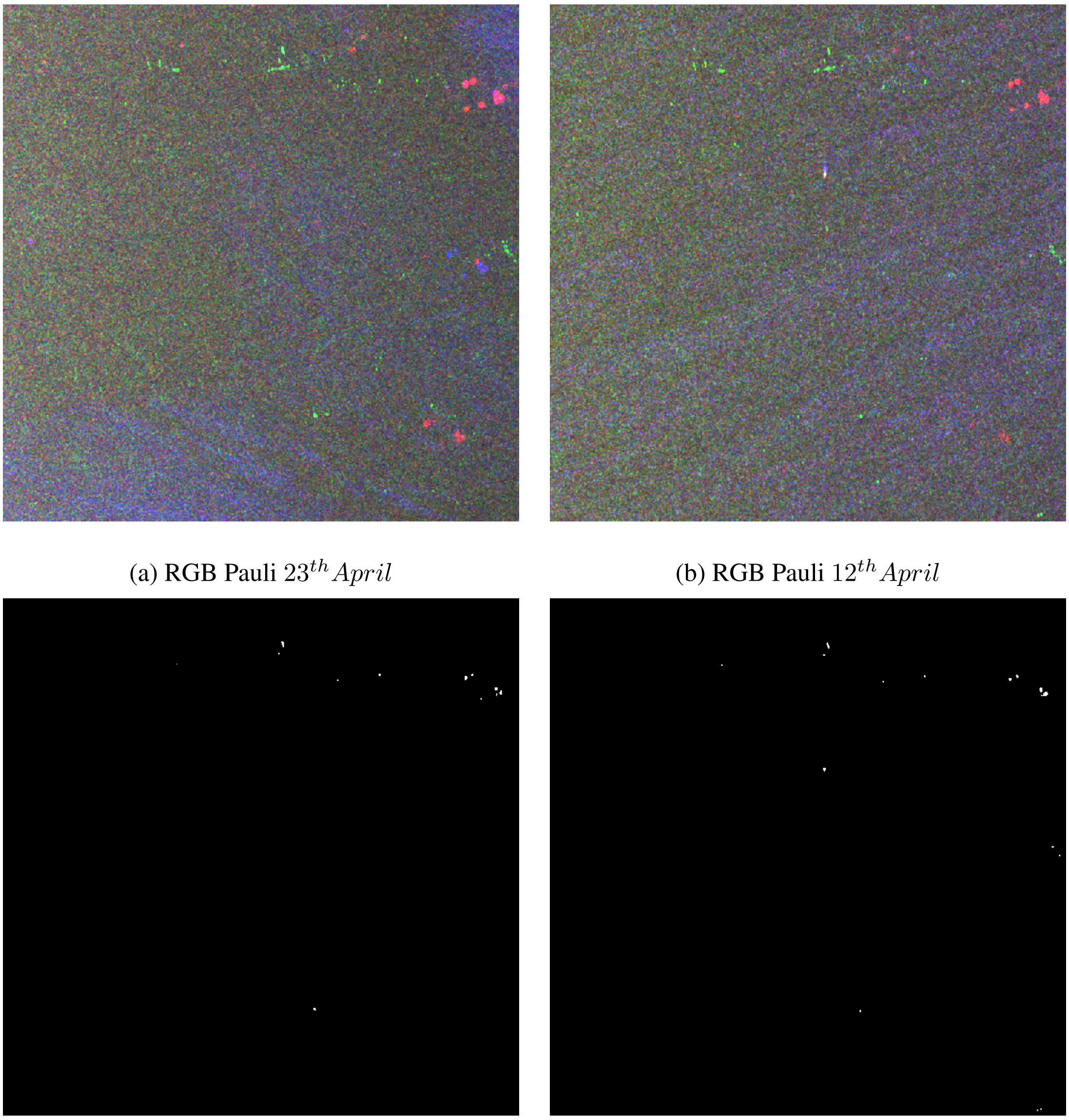

(a) RGB Pauli $23^{th} April$

(b) RGB Pauli $12^{th} April$

(c) Quad-pol GP-PNF $23^{th} April$

(d) Quad-pol GP-PNF $12^{th} April$

Fig. 16. TerraSAR-X quad-pol date over Barcelona harbor (Mediterranean): (a) Crop of RGB Pauli image of $23^{th} April$ (b) Crop of RGB Pauli image of the $23^{th} April$ (c) Detection with GP-PNF Quad-pol $23^{th} April$ (d) Detection with GP-PNF Quad-pol $12^{th} April$.

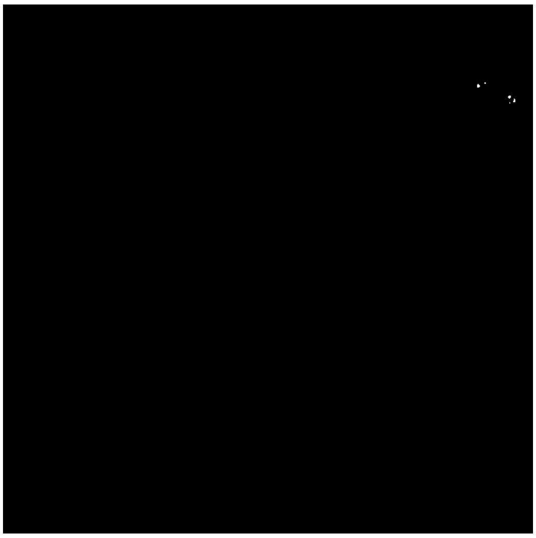

(a) HH/VV GP-PNF $23^{th} April$

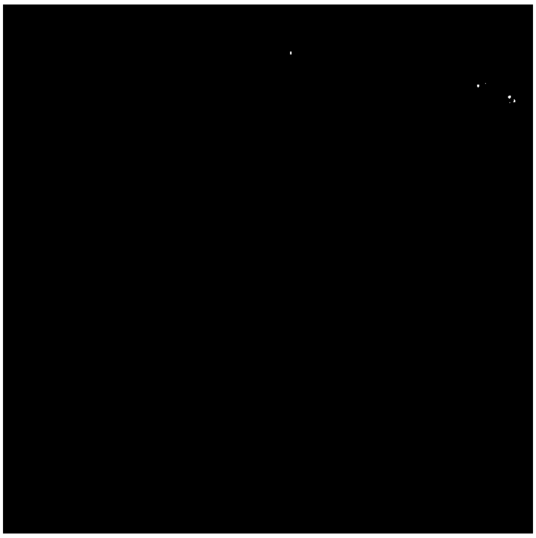

(b) HH/HV GP-PNF $23^{th} April$

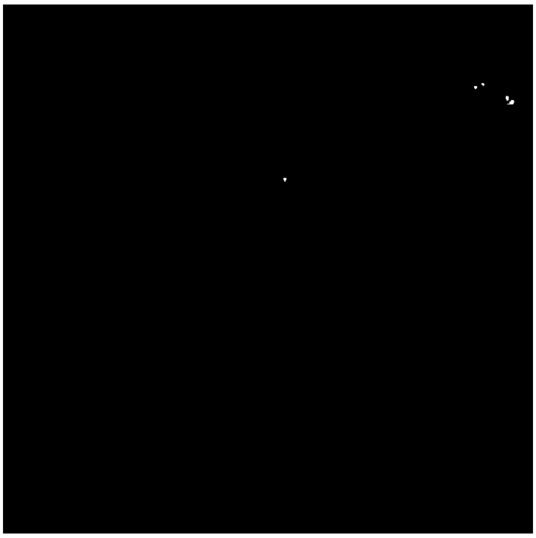

(c) HH/VV GP-PNF $12^{th} April$

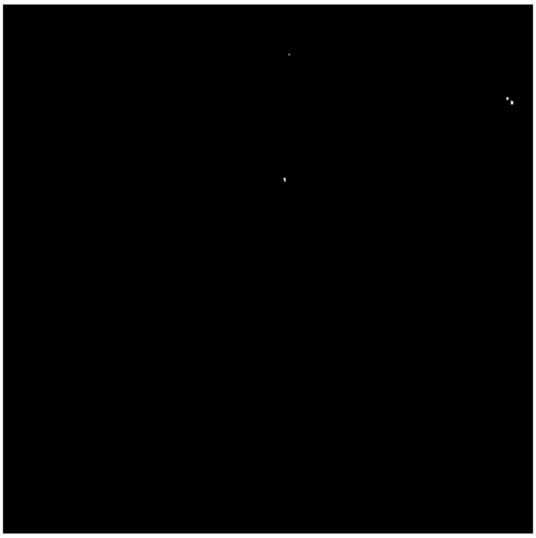

(d) HH/HV GP-PNF $12^{th} April$

Fig. 17. TerraSAR-X over Barcelona harbor (Mediterranean): (a) Dual-pol HH/VV GP-PNF for $23^{th} April$ (b) Dual-pol HH/HV for $23^{th} April$ (c) Dual-pol HH/VV GP-PNF for $12^{th} April$ (d) Dual-pol HH/HV GP-PNF for $12^{th} April$.